Chemosphere 280 (2021) 130764

Contents lists available at ScienceDirect

Chemosphere

journal homepage: www.elsevier.com/locate/chemosphere

A rapid antimicrobial photodynamic water treatment strategy utilizing a xanthene dye with subsequent removal by Goethite Nanoparticles

Sean Doyle [a], Elaine Meade [a], Jinhui Gao [b], Barry O'Hagan [b], John F. Callan [b], Mary Garvey [a], Colin Fowley [a,*]

[a] Department of Life Sciences, Institute of Technology Sligo, Sligo, Ireland
[b] School of Pharmacy, Ulster University, Coleraine, Ireland

ARTICLE INFO

Handling Editor: Y Yeomin Yoon

Keywords:
Nanoparticle water treatment
Nanoparticle residuals
Nanoparticle accumulative toxicity
Photodynamic water treatment
Magnetic nanoparticle water treatment
Goethite nanoparticle

ABSTRACT

Although widely accepted as a water sterilisation technique, chlorination results in the production of potentially harmful by-products, mainly Trihalomethanes. Furthermore, the chlorination process requires specialised infrastructure, management and high costs. In this research paper a potential alternative sterilisation technique was investigated. This rapid three-step process utilized Goethite Nanoparticles and the photosensitising capabilities of a xanthene dye. Rose Bengal (RB) a compound primarily used as a stain to diagnose damaged tissue in the eye was utilized under visible light excitation to sterilise water containing gram-positive *Staphylococcus aureus* and Bacillus cereus. Bacterial reductions (cfu/ml) of up to 6log10 are reported at RB concentrations of 0.5 mg/L and 10 mg/L for *S. aureus* and B. cereus, respectively. Goethite Nanoparticles (GNP's), an iron oxyhydroxide, were synthesised by co-precipitation of iron salts and used to adsorb RB post-sterilisation. Poly-vinyl Alcohol (PVA) functionalised GNP's were synthesised to highlight the adsorbent capabilities of the GNP surface. The adsorption capacity for uncoated GNPs was 476.19 mg/g, this reduced to 170.4 mg/g for PVA-GNP's, highlighting the highly porous nature of the synthesised GNP surface. Adsorption was optimal in slightly acidic conditions (pH5-6). The adsorption parameters best followed Lagergens Pseudo-second order kinetics with correlation coefficients close to unity. At the highest envisaged RB concentration (10 mg/L) approximately 20 mg/L GNP's was required to remove the dye from solution post-treatment. Flame Atomic Absorption analysis of the water post-removal revealed Iron concentrations of 0.058 mg/L. This correlates to removal efficacy of 99.71% with residual iron levels below the EU recommended limit of 0.2 mg/L.

1. Introduction

In terms of water treatment nanomaterial's display some beneficial characteristics due to their high specific surface area and surface reactivity compared to conventional bulk materials (Gupta et al., 2012). The development of engineered nanoparticle water treatment technologies for the removal of heavy metals, microorganisms and organic pollutants has become a diverse branch of nanotechnology in its own right (Ramirez-Muniz et al., 2018). Indeed, the use of nanoparticles (NPs) for water purification is not a new concept with the number of publications in this field increasing yearly in recent decades (Keyhanian et al., 2016). However, the major obstacles of NP water treatment are threefold: (i) recovery of the NP (ii) NP reuse for subsequent treatments and (iii) the unknown accumulative toxicity of these compounds to human and aquatic life.

Over the past few decades, the different phases of iron oxides have been intensely studied across different fields, ranging from wastewater treatment to storage device development. They are of particular interest due to their simple processability, large surface area and their potential for specific surface functionality (Shubair et al., 2018). Iron oxides form different crystalline structures as well as a variety of crystalline phases (Abd El Aal et al., 2019).There are numerous synthetic methods for producing Iron oxide Nanoparticles (IONP's) which include hydrolysis, thermal decomposition, the sol-gel technique and chemical co-precipitation (Petcharoen and Sirivat, 2012). The co-precipitation reaction is perhaps the most feasible method as it can be carried out at Room Temperate and Pressure (RTP) requiring only an $Fe(III)^{+}$ salt as a precursor. Once formed the IONP's can then be wrapped in a particular polymer or biomolecule specific for its intended purpose.

The two most common forms of iron oxide mentioned in the

* Corresponding author. Dept of Life Science, Institute of Technology Sligo, Ash Lane, Sligo, Ireland.
E-mail address: Fowley.colin@itsligo.ie (C. Fowley).

https://doi.org/10.1016/j.chemosphere.2021.130764
Received 1 February 2021; Received in revised form 26 April 2021; Accepted 28 April 2021
Available online 3 May 2021

literature are magnetite (Fe_3O_4) and maghemite (γ-Fe_2O_3). This is in part due to their cubic spinel structure which allows them to possess ferromagnetic abilities at room temperature(Harrison et al., 2002). Haematite (a-Fe_2O_3) is the most common naturally occurring and stable phase of iron oxide and has antiferromagnetic properties due to its corundum crystal structure. These forms of iron oxide are generally non-porous and prior to application in areas such as drug-delivery or wastewater treatment, generally require surface functionalisation. The functionalisation of IONP's with compounds rich in reactive amine groups like chitosan (Khmara et al., 2019) or carboxylates through the use of polyacrylic acid (Sanchez et al., 2018) are most common (Kayal and Ramanujan 2010). designed PVA-functionalised Fe_3O_4 for targeted drug delivery and (Keyhanian et al., 2016) employed a SDS-coating for dye removal from wastewater.

The formation of magnetite (Fe_3O_4) via the co-precipitation method is a relatively simple process, although follows a complex mechanism. The phase transformations of iron oxides are well documented (Peterson et al., 2016), studied the conversion from akageneite to haematite while (Lemine, 2014) converted goethite to haematite through high-energy ball milling. Competent understanding of these phases is crucial as each phase has different structural, morphological, and physical properties which can determine their suitability for specific purposes. A study conducted by (Ahn et al., 2012) determined the distinct phases of iron oxides which occur during the co-precipitation of iron salts to form magnetite. They found that upon first addition of a base, iron oxyhydroxides are the primary product, akageneite being the predominant phase. As the pH was further increased, hydroxide ions replaced chloride ions which were incorporated into the akageneite structure which induced the phase transformation from akageneite to goethite. Goethite is the most thermodynamically stable iron oxyhydroxide in the presence of water(Alexandrov and Rosso, 2014), this coupled with its porous structure and high surface area make it a very appealing adsorbent material. Numerous studies have displayed the ability of goethite as an adsorbent for arsenic from wastewater(Ghosh et al., 2012; Ramirez-Muniz et al., 2018) while (Nassar and Ringsred, 2012) employed goethite as an adsorbent for the removal of Methylene Blue, a pollutant dye arising mainly from the textile industry (Chen et al., 2016; Badeenezhad et al., 2019).

Despite xanthene dyes being regarded as water pollutants, many of them possess unique photosensitising capabilities and are termed photosensitisers. These photosensitisers (PS) are commonly used in Photodynamic Therapy (PDT), a therapeutic method currently used across many medical fields including dermatology and dentistry. The concept is quite simple, requiring 3 ingredients: a photosensitiser (PS), a light source and oxygen(Lee and Baron, 2011). PDT is initiated when light of the correct wavelength illuminates the PS causing electrons to rise to higher energy levels. When that energy is subsequently lost, Type I and Type II reactions occur. Type I photochemical reactions produce free radical oxidative species which are destructive to most cell organelles (Kasimova et al., 2014) and Type II reactions are responsible for the generation of highly reactive singlet oxygen (Demidova and Hamblin, 2005). Activation of a PS and subsequent production of these reactive species while within a cell will almost certainly result in cell destruction (Allison and Moghissi, 2013). The selective and non-resistant nature of this process has resulted in a large increase in its utilisation in microbiology fields termed Antimicrobial Photodynamic Therapy (APDT). The mechanisms by which APDT operates make it unlikely that microorganisms will develop resistance, this coupled with the ease at which it can be carried out make it a very plausible and increasingly utilized antimicrobial technique.

Chlorination is one of the most adapted methods for disinfecting water supplies worldwide due to its performance against common waterborne pathogens. However, during the chlorination process potentially harmful disinfection by-products are formed, most commonly Trihalomethanes and Haloacetic acids (Richardson et al., 2007). There have been over 1000 by-products identified in total as a result of chlorine sterilisation techniques (Zhang et al., 2012). The production of these potentially harmful by-products as well as the specialised infrastructure, management and high costs associated with water chlorination processes justifies the need for research into cheaper, effective alternative methods.

In this work a simple, fast, low-cost method was used for the preparation of porous Goethite Nanoparticles (GNPs) with the potential to adsorb a photosensitiser dye without further functionalisation. The antimicrobial activity of RB, an anionic xanthene compound, was tested on Gram positive medically important *S. aureus* and *B. cereus* bacterial cells in aqueous conditions. The ability of the synthesised GNP's to remove the photosensitiser posttreatment was investigated through adsorption studies. Furthermore, in order to elucidate the sorption ability of the unfunctionalized GNP's, GNP's with Polyvinyl Alcohol (PVA) surface functionalisation were used as a comparison.

2. Materials and methods

2.1. Synthesis of goethite nanoparticles

GNP's were prepared by the chemical co-precipitation of iron (II) salts under oxygen atmosphere and at RTP. Briefly, 10g of Ferric Chloride (Thermo Fisher Scientific, USA) was dissolved in 150 ml ultrapure H_2O and 3.4g Ferrous Sulphate (Sigma Aldrich, USA) was dissolved in 100 ml ultrapure water. Both solutions were mixed and allowed to equilibrate for 10 min. The pH of the resulting solution was ~1. The solution pH was increased by addition of a 25% Sodium Hydroxide (Sigma Aldrich, USA) solution which was added dropwise using a glass pipette and stirred at 600RPM. A dark precipitate started appearing upon first addition of the base. The solution pH was increased to pH2 and no further NaOH was added after this point. The solution was stirred at 600RPM for a further 10mins. The beaker was then placed on a permanent magnet and the precipitate was removed and washed 5 times with ultrapure water before being placed in an oven at 80 °C for 6 h to dry. The resulting product consisted of grey-black crystals which became a brown-red powder when grinded using a mortar and pestle.

2.1.1. PVA functionalisation of GNP's

To obtain surface functionalisation with PVA, nanoparticles were stirred at 600RPM in a 3% w/v PVA (Thermo Fisher Scientific, USA) solution for 12 h. These were then removed, washed 3 times with methanol and dried in an oven at 60 °C for 2 h.

2.2. Characterisation of GNP's & PVA-GNP's

GNP's were characterised for size and surface morphology by X-Ray Diffraction (XRD), Scanning Electron Microscopy (SEM), Fourier-Transfer Infra-Red Spectroscopy (FTIR) and Zeta-Potential.

2.2.1. Powder X-Ray Diffraction

XRD of goethite samples was carried out using a Siemens D-500 X-ray Diffractometer (Siemens, Germany) utilizing Cu Kα radiation (λ = 0.15418 nm) operating at 40 kV and 30 mA with sample rotation from 10° to 80° over 20mins.

2.2.2. Scanning Electron Microscopy

Microstructural analysis was performed at Ulster University's Bio-Imaging Core Facility Unit (Northern Ireland, UK) using a FEI Quanta™ 200 (FEI Company, Eindhoven, the Netherlands) scanning electron microscope operated at an accelerating voltage of 30 kV. The samples were mounted on aluminum stubs using a double-sided adhesive carbon disk and sputter coated with a thin layer (5 nm) of gold/palladium using a Polaron E5100 sputter coating unit (Quorum Technologies Ltd., Sussex, UK). All micrographs were captured using the integrated imaging software xT microscope control and a charge coupled device camera.

2.2.3. Fourier-Transfer Infra-Red Spectroscopy

FTIR analysis was conducted on a PerkinElmer instrument scanning form 4500 cm^{-1} to 450 cm^{-1} for confirmation that PVA molecules had attached to the GNP's surface. The samples were prepared for analysis by the production of KBr discs (KBr- Sigma Aldrich, USA).

2.2.4. Zeta-Potential

The surface charge was determined using a Malvern Zetasizer (Malvern instruments, UK). The surface charge was analysed at ph5, 7 and 9 at 25 °C using a clear zeta-cell and a measurement position of 2 mm. The Zeta-potential of uncoated GNP's ranged from 10 mV in acidic conditions to −29.1 mV in basic conditions with a similar trend seen for PVA-coated GNP's. The isoelectric point is close to neutral with a Zeta-potential of 1.69 mV recorded at pH7 for uncoated GNP's.

2.3. Adsorption studies

2.3.1. pH adsorption dependence

Initial adsorption studies were carried out to determine the optimum pH conditions. Rose Bengal (Thermo Fisher, USA) was used in its disodium salt form. Rose Bengal solution (30 ml, 10 mg/L) was pH adjusted from pH4 to pH11 through careful addition of 0.1 M HCl and 0.1 M NaOH. At each pH condition GNP's (166 mg/L) were added and stirred at 600RPM for 30 min. A sample was collected, centrifuged at 10,000RPM for 2 min before the supernatant was analysed spectrophotometrically using UV–Vis (PerkinElmer, USA) at a wavelength of 549 nm. This allowed the nanoparticle pH adsorption efficiency to be determined. The pH at which maximum adsorption occurred was deemed as 100% efficiency and used to determine the efficiency at the remaining pH conditions.

2.3.2. NP concentration adsorption relationship

The effect of adsorbent dosage was determined using varied NP concentrations of 83 mg/L, 166 mg/L, and 333 mg/L on a fixed RB concentration (10 mg/L). The solution was stirred at 600RPM for 30mins, 1 ml samples were taken at 5-min intervals and prepared for analysis as mentioned previously.

2.3.3. RB concentration adsorption relationship

The effect of initial RB concentration was carried out using a fixed NP dosage of 166 mg/L while varying the initial RB concentration from 10 mg/L to 120 mg/L. The solution was stirred at 600RPM for 30mins with samples taken at 5-min intervals. The samples were collected and prepared for analysis as previously stated.

2.4. Photodynamic Therapy on gram positive S. aureus and B. Cereus

The antimicrobial activity of Rose Bengal was tested on gram positive strains of bacteria, *S. aureus* (ATCC 25293) and B. cereus. Bacterial species were regularly, identity confirmed based on morphological characteristics, biochemical profile and growth on selective agars, specifically PEMBA Bacillus Cereus Medium (Cruinn Diagnostics, Dublin, Ireland)PCR) as per Meade et al., 2019. Strains were stored long term in 20% glycerol at −20 °C and short term in nutrient broth at 5 °C and identity confirmed via Gram stain and selective agars prior to each experimental set up. Bacterial test suspensions containing $1x10^7$cfu/mL were prepared by incubating nutrient broth with a single colony of the test species for 6 h at 37 °C. 10 mL of the bacterial culture was then centrifuged at 10,000 rpm for 10 min and resuspended in sterile PBS. Bacterial suspensions containing a final innocula of ca. $1x10^6$ cfu/mL were then exposed to varying concentrations of Rose Bengal (0.05 mg/L to 10 mg/L) in sterile glass vials, with control suspensions containing PBS without the presence of the photosensitiser. Test suspensions were subsequently incubated at room temperature for 30mins to allow entry of the Rose Bengal into the bacterial cells. The vials were then irradiated with a 20 mW green laser for 15 min before being spread on nutrient agar plates in triplicate. All plates were incubated inverted for 24 h at 37 °C. Surviving colonies were counted and reported as log10 CFU/ml compared to an untreated control. The activity of Rose Bengal was also tested without light irradiation (dark conditions) and compared.

2.5. Fe atomic absorption analysis

Flame Atomic Absorption (Agilent- 280FS AA) analysis was employed to determine if iron leached from the GNP's during dye adsorption and to confirm that no NP's were left suspended in solution following removal using a permanent magnet. Uncoated and PVA-NP's were added to ultrapure water at concentrations of 20 mg/L and 250 mg/L and allowed to stir for 30mins. The samples were then placed above a permanent magnet before samples were taken after 10 min and 30 min and subjected to AA analysis.

3. Results and discussion

3.1. Characterisation

3.1.1. X-Ray Diffraction (XRD)

The XRD spectrum of synthesised Goethite is displayed in Fig. 1. Peaks can be seen at positions of 21.26°, 33.17°, 35.12°, 36.49°, 40.16°, 41.25°, 53.37°, 59.15° and 61.17° which are in similar agreement to JCPDS file for goethite (JCPDS 29–0713). The XRD spectrum is comparable to the XRD spectrum for goethite published by (Ghosh et al., 2012). The spectrum is quite noisy indicating the possible polycrystallinity of the synthesised GNP's. The Scherrer formula (1) was used to determine the average crystallite size:

$$d = \frac{K\lambda}{\beta cos\varnothing} \tag{1a}$$

Where d is the crystal size(nm), λ is the X-ray wavelength (nm), β is the full width at half maximum of the strongest peak; θ is corresponding Bragg angle and K is the Debay-scherrer constant (Petcharoen and Sirivat, 2012). The FWHM of the peaks at 36° was calculated using Origin software and was used to determine crystallite size for both GNP's. The sizes were found to be 8.87 nm and 7.82 nm for the uncoated and PVA-coated GNP's, respectively. This is evident from the slight peak broadening seen on the PVA-GNP spectrum figure S3.

3.1.2. SEM

Fig. 1 displays SEM images of synthesised GNP's and PVA-coated GNP's. It is evident from the images that the particles agglomerate and form clusters. The uncoated GNP's show a variety of particles sizes ranging from approx. 50 nm–550 nm, but most particles are <100 nm. The larger particle sizes are most likely a result of insufficient milling with the mortar and pestle although importantly are still within the nanometre range and applicable for this work.

3.1.3. Fourier-transform infra-red spectroscopy

The FTIR spectrum of goethite, shown in Fig. 2, shows a band at 3341 cm^{-1} that can be assigned to the stretching vibrations of –OH arising from adsorbed water on the surface. The band at 3168 cm^{-1} could be caused by stretching vibrations of –OH groups present in the Goethite structure. A very slight band at 2361 cm^{-1} is the due to adsorbed CO_2 from the atmosphere. The sharp band seen at 1628 cm^{-1} is characteristic of bending vibrations of the –OH groups. The bands at 1202 cm^{-1} and 1128 cm^{-1} are most likely due to adsorbed sulphates arising from the synthesis procedure(Ghosh et al., 2012). The characteristic peaks are present at 880 cm^{-1} and 787 cm^{-1} which indicate the presence of Fe–O–OH bonding while the band at 601 cm^{-1} is a result of Fe–O stretching vibrations. The additional bands in (b) at 2920 cm^{-1}, 1402 cm^{-1}, 1043 cm^{-1} and 922 cm^{-1} verify the attachment of PVA to the GNP's. The very weak bands at 2920 cm^{-1} and 922 cm^{-1} can be

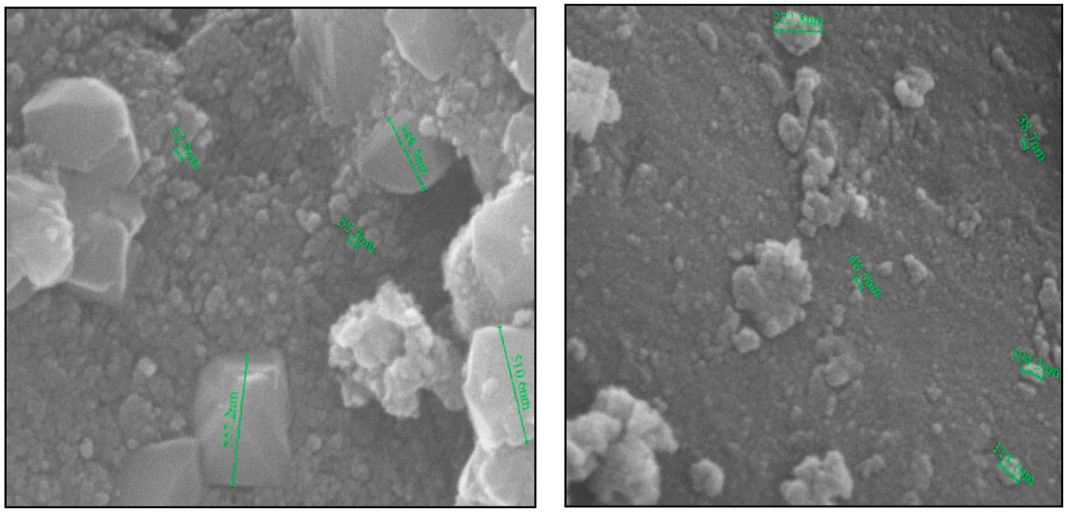

Fig. 1. SEM images (a) uncoated GNP's and (b) PVA-coated GNP's at 100,000x magnification.

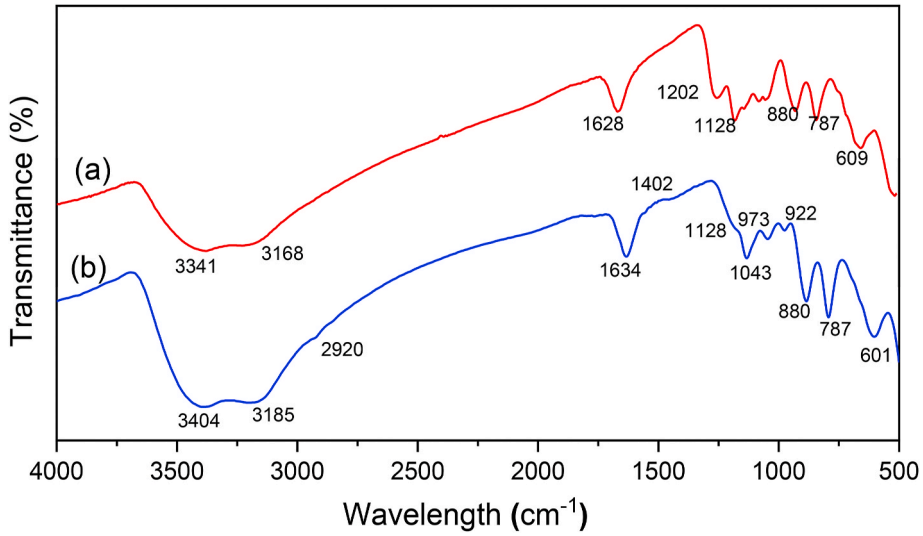

Fig. 2. FTIR spectrum of (a) uncoated GNP's and (b) PVA-coated GNP's. Bands at 2920 cm^{-1}, 1402 cm^{-1}, 1043 cm^{-1} and 922 cm^{-1} confirm attachment of PVA to GNP's.

assigned to C–H stretching and CH_2 rocking vibrations, respectively. The band at 1402 cm^{-1} corresponds to C–C stretching and the slight band at 1043 cm^{-1} is a result of the Fe–O–C bond which enables the attachment of PVA. The wider band in the 3000-3500 cm^{-1} region compared with the uncoated-GNP's spectrum corresponds to the presence of extra –OH groups belonging to PVA..

3.2. Adsorption studies

3.2.1. Effect of pH on adsorbent efficiency

Results displayed in Fig. 3 show that the adsorption efficiency for both coated and uncoated was optimum in acidic conditions. Rose Bengal solution (30 ml, 10 mg/L) was pH adjusted from pH4 to pH11 through careful addition of 0.1 M HCl and 0.1 M NaOH. At each pH condition GNP's bare or PVA coated (166 mg/L) were added and stirred at 600RPM for 30 min. At neutral pH the adsorption efficiency decreased to 93% and 82.7% for the uncoated and PVA-NP's respectively. At pH11 this further decreased to 0% indicating alkaline conditions are unfavourable for anionic dye removal. The reason for this could be the presence of a negative charge on the surface of the NP's at high pH resulting in repulsion of the also negatively charged anionic dye. Noreen et al., reported a similar trend when trying to adsorb an anionic dye using iron oxide from pH 2 to pH11 (Noreen et al., 2020). In extreme acidic conditions (<pH4) Rose Bengal precipitated out of solution. All further experiments were carried out between pH 5–6 which required no adjustment with acid or base as RB is an acidic molecule.

3.2.2. Effect of adsorbent dosage on dye removal

The influence of the adsorbent dose is crucial for adsorption parameters, which was studied in the range of 83–333 mg/L NP conc. at pH5, 25 °C and a constant RB conc. of 10 mg/L. The results in Fig. 5 Fig4 (a) show fast adsorption for uncoated NP's with equilibrium being reached at all 3 concentrations after 5 min. The percentage removal after 5 min at 83 mg/L was 60.81% which increased to 69.76% after 30 min. The reason for the initial rapid adsorption followed by a slower removal when nearing equilibrium can be attributed to the reducing availability of vacant surface sites. Almost 100% removal was seen at 166 mg/L with only 5.16% remaining after 30 min. When the amount of NP's was doubled to 333 mg/L, 100% Rose Bengal removal was recorded after 5 min. At this concentration there is an abundance of adsorption sites for the dye molecules to bind to, resulting in rapid, efficient removal.

Fig. 5 Fig. 4(b) displays that percentage removal using PVA-coated

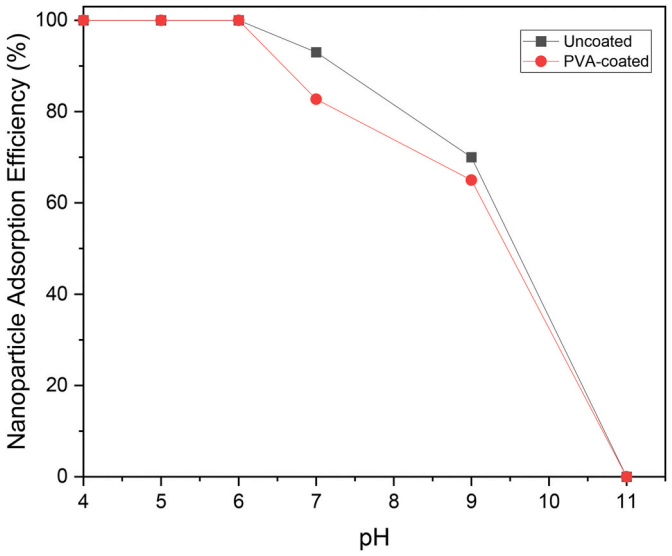

Fig. 3. Adsorption efficiency of uncoated-GNP's and PVA-GNP's ranging from pH4 to pH11 using a RB concentration 10 mg/L, GNP concentration 166 mg/L, 25 °C and stirred at 600RPM for 30 min..

NP's was significantly reduced with 61.2% removal after 30 min at 333 mg/L. Only 10.5% removal after 30 min was recorded at 83 mg/L, almost 6-fold less than the uncoated NP's at the same concentration. This could be due to the PVA molecules occupying a large amount of the adsorption sites on the nanoparticle surface. If the adsorbent dosage is too high, it can have an adverse effect on removal efficiency due to agglomeration of NP's which ultimately decreases the availability of surface adsorption sites (Shubair et al., 2018). This could explain why there is little difference between the 166 mg/L and 333 mg/L adsorption efficiencies in Fig. 2(b) despite a doubling in adsorbent concentration. It is also clear that the rate at which the RB is removed is slower. Rather than rapid adsorption in the first 5 min, the RB removal occurs slowly and uniformly over 20 min before beginning to level off at equilibrium. A possible explanation for this could be the steric hindrance caused by the surface PVA molecules which slows the process of the dye molecules reaching available adsorption sites on the NP surface. Based on these results a NP concentration of 166 mg/L was used to study the effect of dye concentration.

3.2.3. *Effect of dye concentration on adsorption*

Fig. 6 displays the effect of increasing the RB concentration from 10 mg/L up to 120 mg/L using a fixed adsorbent dosage of 166 mg/L. After 30mins the RB removal dropped from 99.24% at 10 mg/L to 64.95% at 120 mg/L for the uncoated GNP's. This can be explained by the increased amount of dye molecules with no increase in active sites. When the saturation point has been reached no active sites are available

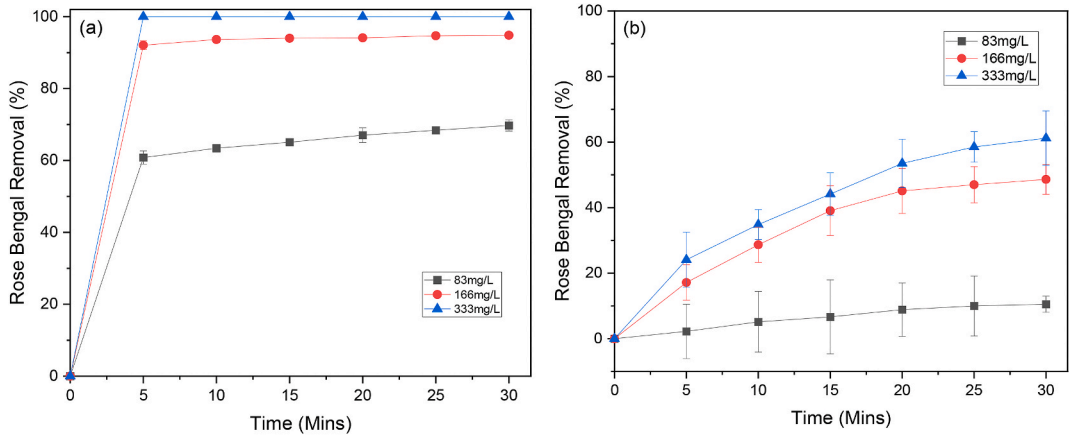

Fig. 4. (a) and (b): The effect of varying the concentrations of Uncoated (a) and PVA-coated NP's (b) on Rose Bengal Removal efficiency. (Rose Bengal concentration was kept constant at 10 mg/L, pH5 and carried out at 25 °C).

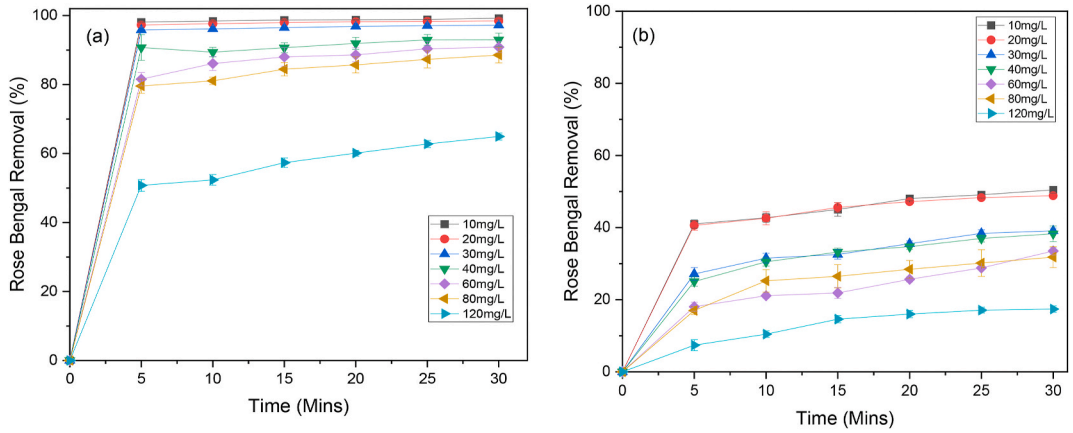

Fig. 5. The effect of varying initial RB concentration on removal efficiency using (a) uncoated-GNP's and (b) PVA-GNP's at a fixed GNP concentration (166 mg/L) stirred at 600RPM, 25 °C and pH5.

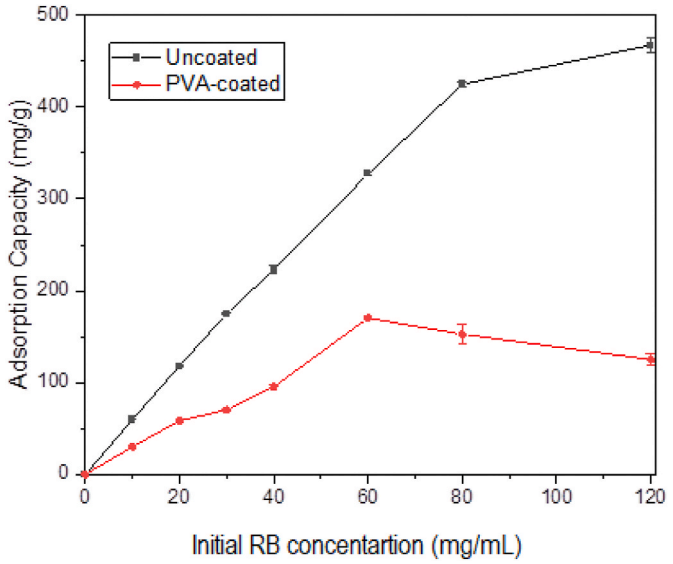

Fig. 6. The adsorption capacity of both uncoated and PVA-coated IONP's at initial RB concentrations ranging from 10 mg/L to 40 mg/L.

for surface binding and no further adsorption takes place. The PVA-coated IONP's removed 17.4% of the RB at 120 mg/L which highlights the superior adsorbent capabilities of the uncoated GNP's.

Fig. 6 displays a plot of adsorption capacity (mg/g) against initial RB concentration (mg/L). The plots indicate that as the initial RB concentration increased from 10 mg/L to 80 mg/L the adsorption capacity of the uncoated GNP's increased linearly, when the concentration increased above 80 mg/L the adsorption capacity levelled off suggesting that all active sites are occupied,; and the NP's are therefore saturated. The maximum adsorption capacity recorded for the uncoated GNP's at 120 mg/L was 467.62 mg/g. The adsorption capacity of the PVA-GNP's increased gradually between initial RB concentrations 10 mg/L to 60 mg/L, reaching a capacity of 170.4 mg/g. When the initial RB concentration increased above 60 mg/L the adsorption capacity decreased slightly for PVA-GNP's, falling to 125.28 mg/g at 120 mg/g. An explanation for this is at higher RB concentrations (>60 mg/L) there is an abundance of molecules competing for adsorption sites which results in a 'blockage' between the PVA strands which essentially acts as a pathway to the GNP surface. This 'blockage' ultimately results in less RB molecules reaching the adsorption sites on the surface and thus a lower adsorption capacity. At 40 mg/L the adsorption capacities were 223.21 mg/g and 95.47 mg/g for both the uncoated and PVA-coated NP's respectively. This would indicate that the PVA-coating reduces adsorption capabilities of the NP's by almost 60%. Interestingly, despite Fig. 6 (a) showing that Rose Bengal removal decreased at the higher initial RB concentrations the adsorption capacity increased as concentration increased. An explanation for this is that the driving force for absorption of the RB molecules onto the NP's surface is increased at higher concentrations which forces equilibrium towards adsorption (Chen et al., 2016). This driving force is crucial to overcome all mass transfer resistances of the RB transitioning from the aqueous phase to the solid phase(Hameed et al., 2008). A similar trend was reported by (Badeenezhad et al., 2019) when adsorbing Methylene Blue from aqueous solution. Fig. 6 also highlights the impact PVA coating has on the absorption capabilities of the GNPs. PVA coatings are routinely utilized to enhance the stability of various nano particles. However, NP surface interactions would appear to be the driving force behind the absorption capabilities of the GNP. Therefore, the PVA coating shields this surface from the surrounding environment and therefore impedes the absorption of RB from that environment.

3.3. Adsorption kinetics

3.3.1. Pseudo-first and second order kinetics

The kinetics of RB adsorption onto the uncoated and PVA-coated GNP's was analysed using pseudo first-order, pseudo second-order and Webers intraparticle diffusion kinetic models. The linearised lagergren pseudo-first order reaction is represented in equation (2).

$$\ln(qe - qt) = \ln qe - k_i t \tag{2}$$

where q_e (mg/g) is the amount of solute adsorbed at equilibrium, q_t is the amount of solute adsorbed at time (t) and k_1 is the first-order rate constant (min^{-1}). The data was plotted as *ln(qe-qt) vs. t* and did not fit the first-order rate equation with correlation coefficients well below 1 suggesting the reaction does not follow first-order kinetics. The linearised lagergren pseudo second-order kinetics reaction is represented in equation (3).

$$\frac{t}{qt} = \frac{t}{k_2 qe^2} + \frac{1}{qe}\, t \tag{3}$$

Where k_2 is the second-order rate constant (g. mg. min^{-1}). If *h* is the initial adsorption rate ($h=k_2qe^2$) then equation (4) becomes:

$$\frac{t}{qt} = \frac{1}{h} + \frac{1}{qe} \tag{4}$$

After plotting the data, $qe_{calculated}$, k_2 and *h* can all be determined. Fig. 7 displays the plot of pseudo second-order reaction of uncoated GNP's, t/qt *vs. t* and the kinetic parameters are listed in Table 1. The conformity of calculated qe values to experimental qe values coupled with R^2 values of 1 suggest that the adsorption of RB dye onto Fe_2O_3 nanoparticles follows a chemisorption mechanism via electrostatic attraction (Keyhanian et al., 2016). The assumption would be that the sorption ability of the IONP's is proportional to the number of absorption sites on their surface relating to the chemical sorption theory (Zhang et al., 2018). The mechanism of the RB adsorbing to the porous sites on the nanoparticles is a multi-step process. The data for PVA-GNP's also best fits pseudo-second order rate kinetics with R^2 values near conformity, suggesting that adsorption also follows a chemisorption mechanism. PVA-GNP's were purposely used to highlight the adsorption capabilities of the goethite surface, because of this further kinetic modelling was only applied to uncoated GNP experimental data. To analyse the mechanisms of adsorption, the experimental

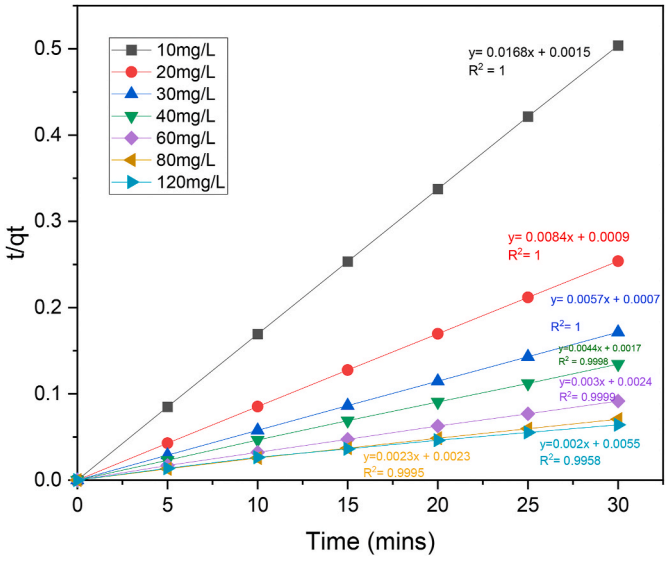

Fig. 7. Pseudo second-order kinetics plot of experimental data for Uncoated GNP's.

Table 1
Kinetics Parameters from Psuedo Second-Order reaction for uncoated-GNP's.

Initial RB Conc. (mg/L)	K_2 (g. mg^{-1}. Min^{-1})	qe_{calc} (mg/g)	qe_{exp} (mg/g)	h (mg. g^{-1}. Min^{-1})	R^2
10	0.18816	59.52	59.544	666.66	1
20	0.0784	119.04	118.156	1111.11	1
30	0.0464	175.44	174.96	1428.571	1
40	0.0114	227.27	223.208	588.23	0.9998
60	0.00375	333.33	327.132	416.66	0.9999
80	0.0023	434.78	425.04	434.78	0.9995
120	0.00073	500	467.616	181.82	0.9958

data was plotted using Webers intra-particle diffusion model.

3.3.2. Intraparticle diffusion model

The mechanism of adsorption can be divided into 4 stages: 1) the mass transfer driving force 2) Boundary-layer Diffusion, 3) dye attachment to adsorption sites and 4) intraparticle diffusion (Plazinski and Rudzinski, 2009). The slowest of these stages determines the over-all rate of adsorption. Webers intra-particle diffusion model is described in equation (4).

$$Q_t = kid\, t^{½} + C \tag{1b}$$

Where Qt (mg/g) is the amount of solute adsorbed at time, *t*, K*id* (mg. g^{-1}.$min^{-1/2}$) is the intra-particle diffusion constant and C was a constant, which specifies the depth of layer boundary(Noreen et al., 2020). Their values can be determined from a plot of qt *vs.* $t^{1/2}$, displayed in Fig. 8. The R^2 values are close to unity at all RB concentrations with the exception of 40 mg/L, which indicates the appropriateness of this model. This confirms the occurrence of an intraparticle diffusion process. If the plots pass through the origin it could be concluded that the intraparticle diffusion process is the only rate-limiting step(Naushad et al., 2016). As evident from Fig. 8 the plots do not pass through the origin so it can be determined that intraparticle diffusion is not the only rate limiting step and at least 1 of the other 4 stages mentioned have a role in limiting the rate of adsorption.

3.3.3. Adsorption isotherms

The performance of an adsorbent can be assessed by adsorption isotherm data generated by experimental data. The isotherm data can be modelled to predict and compare the adsorption performance, this is a crucial aspect for adsorption experiment design (Fu et al., 2015). The data was fitted to the Langmuir and Freundlich models which are expressed linearly in Equations (5) and (6):

$$\frac{Ce}{Qe} = \frac{1}{QmKL} + \frac{Ce}{Qm} \tag{5}$$

$$Log\,(Q_e) = Log\,(k_f) + \frac{1}{n} + Log(C_e) \tag{6}$$

Where Q_e is the amount of RB adsorbed on GNP's (mg/g), C_e is the equilibrium concentration of RB in the supernatant (mg/L), K_L is the Langmuir equilibrium adsorption constant (L/mg), Q_m is the maximum adsorbed amount of RB per mass of goethite for complete monolayer coverage (mg/g), K_F is the Freundlich constant relating to the adsorption capacity [(mg/g)(L/mg)$^{1/n}$] and 1/n is the adsorption intensity factor (unitless)(Nassar and Ringsred, 2012). The data best fits the Langmuir model indicating that adsorption of RB on GNP's surface by a monolayer coverage and that forces of interaction between adsorbed species are negligible(Noreen et al., 2020). Isotherm parameters for Langmuir and Freundlich models are presented in Table 2. The Q_m value observed for adsorption of RB onto GNP's is higher than the values reported by similar studies (Naushad et al., 2016), recorded a Q_m of 142.86 mg/g using amberlite resin to remove RB while (Gupta et al., 2012) presented a Q_m of 6.68x10^{-5} mol^{-1} g^{-1} (37.5 mg/g) using bottom-ash as the adsorbent to remove RB.

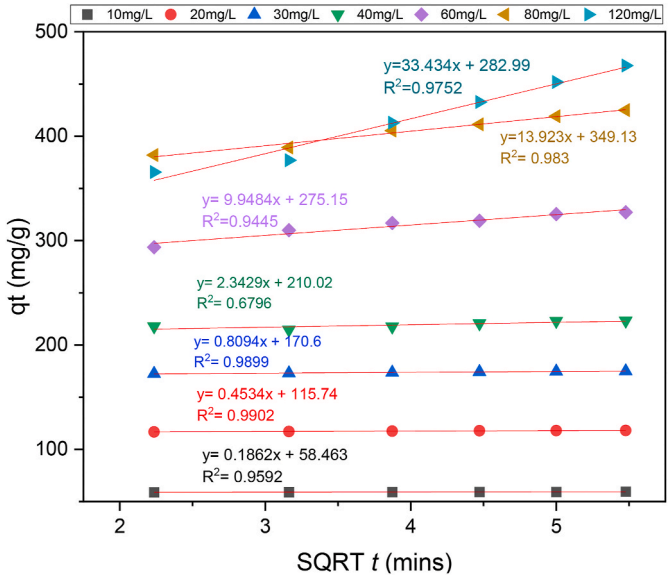

Fig. 8. Webers intra-particle diffusion model applied to experimental data for uncoated GNP's.

3.4. Antimicrobial Photodynamic Therapy

The antimicrobial ability of Rose Bengal was assessed on 2 g-positive bacteria, *S. aureus* and *B. cereus.* Photodynamic Therapy was carried out in an aqueous condition to replicate a water treatment setting, results are displayed in Fig. 9. It is well documented that photosensitising dyes, including Rose Bengal, are non-cytotoxic without activation by light. This is evident at concentrations ranging from 0.05 mg/L to 0.5 mg/L relating to *S. aureus,* while a higher concentration of 10 mg/L was non-lethal to *B. cereus* without photon activation. Rose Bengal (λ_{max} = 549 nm) was activated using a 20 mW green laser (520–560 nm) for 15 min. With regards to *S. aureus*, a 0.8 log_{10}, 2.64 log_{10} and 6 log_{10} (cfu/ml) reduction was seen at RB concentrations of 0.05 mg/L, 0.1 mg/L and 0.5 mg/L, respectively. At the same concentrations, a 1.57 log_{10}, 1.69 log_{10} and 2.09log_{10} (cfu/ml) reduction occurred for *B. cereus.* A RB concentration of 10 mg/L was required to produce a 5.84log_{10} cfu/ml reduction, 20 times the concentration needed for a similar reduction on *S. aureus* cells. Upon light activation while within the bacterial cells highly reactive singlet oxygen and free radicals are generated resulting in cell death (Nagahara et al., 2013). These results indicate that water contaminated with high concentrations of up to 6log_{10} of *S. aureus* and *B. cereus,* can be effectively sterilized with moderately low concentrations of RB in conjunction with visible light activation.

3.5. Iron analysis of treated water samples

To determine residual iron levels, post Treatment flame atomic absorption studies were conducted on both PVA coated and bare GNPs. Results of this analysis are displayed in Fig. 10. At the higher concentration of 250 mg/L the Fe concentration after 30mins reaches 0.767

Table 2
Isotherm Parameters relating to experimental data of uncoated-GNP's linked to the Langmuir and Freundlich models.

Langmuir model			Freundlich Model		
K_L (L/mg)	Q_m (mg/g)	R_2	K_F [(mg/g)(L/mg)$^{1/n}$]	1/n (unitless)	R_2
0.6	476.19	0.996	166.802	0.337	0.9569

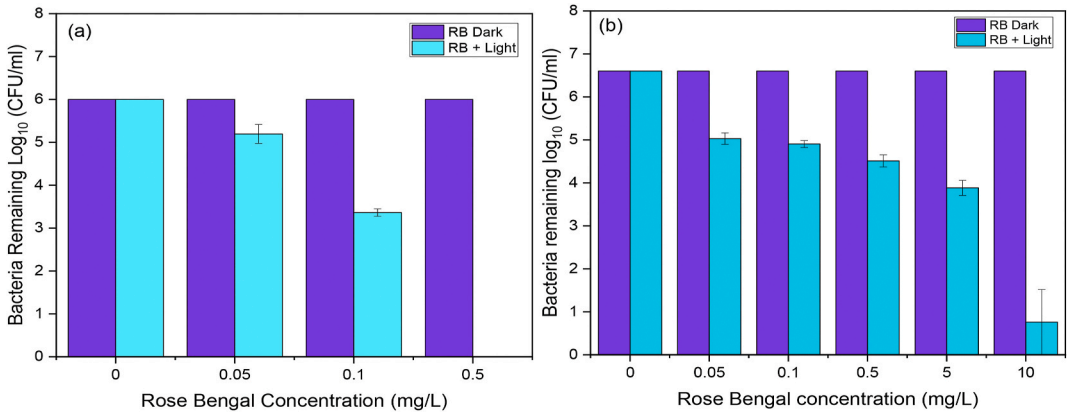

Fig. 9. Amount of Bacteria remaining as a function of Log10 (CFU/ml) following Antimicrobial Photodynamic Therapy on (a) S. Aureus cells and (b) B. Cereus cells at a range of RB concentrations in both illuminated and dark conditions.

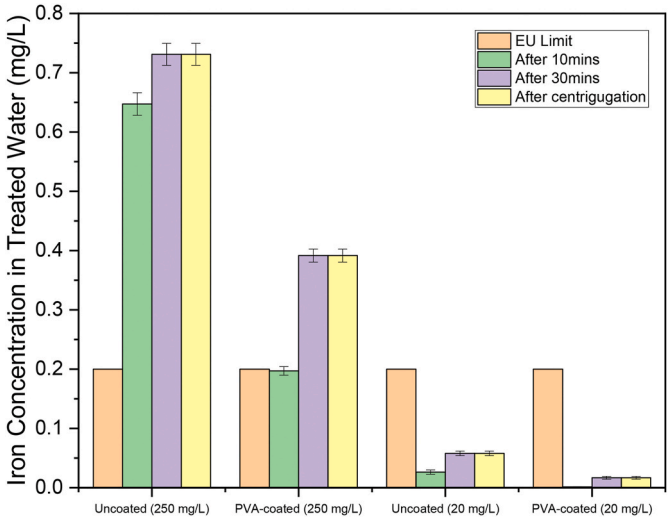

Fig. 10. Atomic Absorption analysis of water samples following treatment with Uncoated and PVA-coated NP's at 20 mg/L and 250 mg/L.

mg/L and 0.409 mg/L for the uncoated and PVA-coated GNP's, respectively. An explanation for the lower value for the PVA-GNP's is the polymer coating passivates the NP surface preventing the leaching of Fe ions. This coating prevents iron leaching from the NP surface as interaction with the surrounding environment is impeded. However, although imposing a greater level of stability this passivation impedes the ability of the GNP to remove the dye post treatment. When considering the time frame required for removal and the level of iron leaching from bare GNPs the need for PVA coating is hard to justify.

When a NP conc. of 20 mg/L is used these values fall to 0.058 mg/L and 0.017 mg/L which is well below the EU limit of 0.2 mg/L. Based on the adsorption studies it is unlikely that GNP concentrations of over 20 mg/L would be required to remove moderate levels of RB dye in aqueous solution. There is no drop in Fe concentration when the sample after 30mins was centrifuged which indicates that the majority of GNP's were adequately removed via a permanent magnet placed below the solution. When 20 mg/L uncoated goethite was added only 0.058ug/L of Fe was detected post-treatment which indicates a removal efficiency of 99.71%. Applying the maximum adsorption capacity of uncoated-GNP's to the APDT data would suggest that a GNP concentration of 21.29 mg/L would be required to adequately remove the 10 mg/L RB concentration required for the highest reduction of B. Cereus. Further comparison of the Flame Atomic Absorption data in Fig. 10 suggests that iron levels in the water post-treatment under the aforementioned conditions would be considerably below the EU limit of 0.2 mg/L. Fig. 10

4. Conclusions

In this study Goethite Nanoparticles were synthesised using a fast, simple, low-cost method for the adsorption of Rose Bengal dye from water. Goethite Nanoparticles functionalised with Polyvinyl Alcohol were also synthesised to highlight the adsorption capabilities of the Goethite surface. Adsorption was best suited to slightly acidic conditions (pH5-6) while an increase in initial RB concentration correlated to an increase of adsorption capacity (mg/g) up to 120 mg/L for uncoated and 60 mg/L for PVA-coated. The maximum adsorption capacity for uncoated GNP's was 467.62 mg/g and 170.4 mg/g for PVA-GNP's. Adsorption of Rose Bengal onto the Goethite surface followed Pseudo-second order kinetics and best fit the Langmuir isotherm model suggesting attachment is via chemisorption and follows a monolayer coverage. Rose Bengal is also a potent photosensitiser displayed by antimicrobial Photodynamic Therapy on 2 g-positive bacteria *S. aureus* and *B. cereus* with concentrations of 0.5 mg/L and 10 mg/L required for $6\log_{10}$ reductions, respectively. Elemental analysis of treated water showed that an appropriate GNP dose required for the adsorption of 10 mg/L RB from a water sample resulted in no major leachates of iron ions, with Fe levels of 0.058 mg/L recorded post removal via a permanent magnet. Considerably lower than the EU limit of 0.2 mg/L. These results suggest that the use of APDT in conjunction with GNPs as a water sterilisation technique is potentially viable and warrants further investigation on its effectiveness against alternative organisms.

Declaration of competing interest

The authors declare that they have no known competing financial interests or personal relationships that could have appeared to influence the work reported in this paper.

Appendix A. Supplementary data

Supplementary data to this article can be found online at https://doi.org/10.1016/j.chemosphere.2021.130764.

References

Ahn, T., Kim, J.H., Yang, H.M., Lee, J.W., Kim, J.D., 2012. Formation pathways of magnetite nanoparticles by coprecipitation method'. J. Phys. Chem. C 116 (10), 6069–6076. https://doi.org/10.1021/jp211843g available:

Alexandrov, V., Rosso, K.M., 2014. Electron transport in pure and substituted iron oxyhydroxides by small-polaron migration. J. Chem. Phys. 140 (23) https://doi.org/10.1063/1.4882065 available:

Allison, R.R., Moghissi, K., 2013. Oncologic photodynamic therapy: clinical strategies that modulate mechanisms of action. Photodiagnosis Photodyn. Ther. 10 (4), 331–341. https://doi.org/10.1016/j.pdpdt.2013.03.011 available:

Badeenezhad, A., Azhdarpoor, A., Bahrami, S., Yousefinejad, S., 2019. Removal of methylene blue dye from aqueous solutions by natural clinoptilolite and clinoptilolite modified by iron oxide nanoparticles. Mol. Simulat. 45 (7), 564–571. https://doi.org/10.1080/08927022.2018.1564077 available:

Chen, D., Zeng, Z.Y., Zeng, Y.B., Zhang, F., Wang, M., 2016. Removal of methylene blue and mechanism on magnetic gamma-Fe2O3/SiO2 nanocomposite from aqueous solution. Water Resources and Industry 15, 1–13. https://doi.org/10.1016/j.wri.2016.05.003 available:

Demidova, T.N., Hamblin, M.R., 2005. Photodynamic inactivation of Bacillus spores, mediated by phenothiazinium dyes. Appl. Environ. Microbiol. 71 (11), 6918–6925. https://doi.org/10.1128/aem.71.11.6918-6925.2005 available:

Fu, J.W., Chen, Z.H., Wang, M.H., Liu, S.J., Zhang, J.H., Zhang, J.N., Han, R.P., Xu, Q., 2015. Adsorption of methylene blue by a high-efficiency adsorbent (polydopamine microspheres): kinetics, isotherm, thermodynamics and mechanism analysis. Chem. Eng. J. 259, 53–61. https://doi.org/10.1016/j.cej.2014.07.101 available:

Ghosh, M.K., Poinern, G.E.J., Issa, T.B., Singh, P., 2012. Arsenic adsorption on goethite nanoparticles produced through hydrazine sulfate assisted synthesis method. Kor. J. Chem. Eng. 29 (1), 95–102. https://doi.org/10.1007/s11814-011-0137-y available:

Gupta, V.K., Mittal, A., Jhare, D., Mittal, J., 2012. Batch and bulk removal of hazardous colouring agent Rose Bengal by adsorption techniques using bottom ash as adsorbent. RSC Adv. 2 (22), 8381–8389. https://doi.org/10.1039/c2ra21351f available:

Hameed, B.H., Mahmoud, D.K., Ahmad, A.L., 2008. Equilibrium modeling and kinetic studies on the adsorption of basic dye by a low-cost adsorbent: coconut (Cocos nucifera) bunch waste. J. Hazard Mater. 158 (1), 65–72. https://doi.org/10.1016/j.jhazmat.2008.01.034 available:

Harrison, R.J., Dunin-Borkowski, R.E., Putnis, A., 2002. Direct imaging of nanoscale magnetic interactions in minerals. Proc. Natl. Acad. Sci. U. S. A 99 (26), 16556–16561. https://doi.org/10.1073/pnas.262514499 available:

Kasimova, K.R., Sadasivam, M., Landi, G., Sarna, T., Hamblin, M.R., 2014. Potentiation of photoinactivation of Gram-positive and Gram-negative bacteria mediated by six phenothiazinium dyes by addition of azide ion. Photochem. Photobiol. Sci. 13 (11), 1541–1548. https://doi.org/10.1039/c4pp00021h available:

Kayal, S., Ramanujan, R.V., 2010. Doxorubicin loaded PVA coated iron oxide nanoparticles for targeted drug delivery. Materials Science & Engineering C-Materials for Biological Applications 30 (3), 484–490. https://doi.org/10.1016/j.msec.2010.01.006 available:

Keyhanian, F., Shariati, S., Faraji, M., Hesabi, M., 2016. Magnetite nanoparticles with surface modification for removal of methyl violet from aqueous solutions. Arabian Journal of Chemistry 9, S348–S354. https://doi.org/10.1016/j.arabjc.2011.04.012 available:

Khmara, I., Strbak, O., Zavisova, V., Koneracka, M., Kubovcikova, M., Antal, I., Kavecansky, V., Lucanska, D., Dobrota, D., Kopcansky, P., 2019. Chitosan-stabilized iron oxide nanoparticles for magnetic resonance imaging. J. Magn. Magn Mater. 474, 319–325. https://doi.org/10.1016/j.jmmm.2018.11.026 available:

Lee, Y., Baron, E.D., 2011. Photodynamic therapy: current evidence and applications in dermatology. Semin. Cutan. Med. Surg. 30 (4), 199–209. https://doi.org/10.1016/j.sder.2011.08.001 available:

Lemine, O.M., 2014. Transformation of goethite to hematite nanocrystallines by high energy ball milling. In: Advances in Materials Science and Engineering, 2014. https://doi.org/10.1155/2014/589146 available:

Nagahara, A., Mitani, A., Fukuda, M., Yamamoto, H., Tahara, K., Morita, I., Ting, C.C., Watanabe, T., Fujimura, T., Osawa, K., Sato, S., Takahashi, S., Iwamura, Y., Kuroyanagi, T., Kawashima, Y., Noguchi, T., 2013. Antimicrobial photodynamic therapy using a diode laser with a potential new photosensitizer, indocyanine green-loaded nanospheres, may be effective for the clearance of Porphyromonas gingivalis. J. Periodontal. Res. 48 (5), 591–599. https://doi.org/10.1111/jre.12042 available:

Nassar, N.N., Ringsred, A., 2012. Rapid adsorption of methylene blue from aqueous solutions by goethite nanoadsorbents. Environ. Eng. Sci. 29 (8), 790–797. https://doi.org/10.1089/ees.2011.0263 available:

Naushad, M., Alothman, Z.A., Awual, M.R., Alfadul, S.M., Ahamad, T., 2016. Adsorption of rose Bengal dye from aqueous solution by amberlite Ira-938 resin: kinetics, isotherms, and thermodynamic studies. Desalination and Water Treatment 57 (29), 13527–13533. https://doi.org/10.1080/19443994.2015.1060169 available:

Noreen, S., Mustafa, G., Ibrahim, S.M., Naz, S., Iqbal, M., Yaseen, M., Javed, T., Nisar, J., 2020. Iron oxide (Fe2O3) prepared via green route and adsorption efficiency evaluation for an anionic dye: kinetics, isotherms and thermodynamics studies. Journal of Materials Research and Technology-Jmr&T 9 (3), 4206–4217. https://doi.org/10.1016/j.jmrt.2020.02.047 available:

Petcharoen, K., Sirivat, A., 2012. Synthesis and characterization of magnetite nanoparticles via the chemical co-precipitation method'. Materials Science and Engineering B-Advanced Functional Solid-State Materials 177 (5), 421–427. https://doi.org/10.1016/j.mseb.2012.01.003 available:

Peterson, K.M., Heaney, P.J., Post, J.E., 2016. A kinetic analysis of the transformation from akaganeite to hematite: an in situ time-resolved X-ray diffraction study. Chem. Geol. 444, 27–36. https://doi.org/10.1016/j.chemgeo.2016.09.017 available:

Plazinski, W., Rudzinski, W., 2009. Kinetics of adsorption at solid/solution interfaces controlled by intraparticle diffusion: a theoretical analysis. J. Phys. Chem. C 113 (28), 12495–12501. https://doi.org/10.1021/jp902914z available:

Ramirez-Muniz, K., Perez-Rodriguez, F., Rangel-Mendez, R., 2018. Adsorption of arsenic onto an environmental friendly goethite-polyacrylamide composite. J. Mol. Liq. 264, 253–260. https://doi.org/10.1016/j.molliq.2018.05.063 available:

Richardson, S.D., Plewa, M.J., Wagner, E.D., Schoeny, R., DeMarini, D.M., 2007. Occurrence, genotoxicity, and carcinogenicity of regulated and emerging disinfection by-products in drinking water: a review and roadmap for research. Mutat. Res. Rev. Mutat. Res. 636 (1–3), 178–242. https://doi.org/10.1016/j.mrrev.2007.09.001 available:

Sanchez, L.M., Martin, D.A., Alvarez, V.A., Gonzalez, J.S., 2018. Polyacrylic acid-coated iron oxide magnetic nanoparticles: the polymer molecular weight influence. Colloid. Surface. Physicochem. Eng. Aspect. 543, 28–37. https://doi.org/10.1016/j.colsurfa.2018.01.050 available:

Shubair, T., Eljamal, O., Khalil, A.M.E., Tahara, A., Matsunaga, N., 2018. Novel application of nanoscale zero valent iron and bimetallic nano-Fe/Cu particles for the treatment of cesium contaminated water. Journal of Environmental Chemical Engineering 6 (4), 4253–4264. https://doi.org/10.1016/j.jece.2018.06.015 available:

Zhang, H.F., Zhang, Y.H., Shi, Q., Hu, J.Y., Chu, M.Q., Yu, J.W., Yang, M., 2012. Study on transformation of natural organic matter in source water during chlorination and its chlorinated products using ultrahigh resolution mass spectrometry. Environ. Sci. Technol. 46 (8), 4396–4402. https://doi.org/10.1021/es203587q available:

Zhang, Z.X., Liu, H.B., Lu, P., Chen, T.H., Ma, W.J., 2018. Nanostructured alpha-Fe2O3 derived from siderite as an effective Hg(II) adsorbent: performance and mechanism. Appl. Geochem. 96, 92–99. https://doi.org/10.1016/j.apgeochem.2018.06.016 available: